TURBULENT FLOW OVER WETTED AND NON-WETTED SUPERHYDROPHOBIC COUNTERPARTS WITH RANDOM STRUCTURE

B. Vajdi Hokmabad[1], S. Ghaemi[1,a)]

[1] *Department of Mechanical Engineering, University of Alberta, Edmonton, Alberta T6G 2G8, Canada*

The turbulent structure of a channel flow over a non-wetted superhydrophobic (SHO) surface is experimentally investigated at Re = 9,600 (based on channel width) at the region of $y^+>10$ within the buffer and logarithmic layers. The SHO surface has a random pattern produced by spray coating and is compared with a wetted counterpart and also a smooth surface. Two planar particle image velocimetry (PIV) measurements are carried out in the streamwise/spanwise and streamwise/wall-normal planes. The vector fields are obtained from both ensemble averaging and individual cross-correlations of double-frame images. The results showed a small increase (~5%) of the mean velocity profile at $y^+=10$ over the non-wetted surface in comparison with the wetted and the smooth surfaces. Up to 15% reduction of normal and shear Reynolds stresses is observed in the inner layer over the non-wetted SHO surface. The wetted SHO counterpart demonstrates no effect on the mean velocity and Reynolds stresses in comparison with the smooth surface. The result confirms the comment of Gad-el-Hak [Phys. Fluids 25, 025103 (2013)] that the wetted SHO is hydrodynamically smooth if the surface pores are smaller than the viscous sublayer thickness. A noticeable suppression of the sweep and ejection events, increase of the spanwise spacing of the low and high speed streaks, and attenuation of vortical structures are observed over the non-wetted SHO. These indicate attenuation of the turbulence regeneration cycle due to the slip boundary condition over the non-wetted SHO surfaces with random texture.

Author to whom correspondence should be addressed. Electronic mail: ghaemi@ualberta.ca.

I. INTRODUCTION

The friction force between the turbulent flow and the solid surface is the main source of energy loss in long transmission pipelines. The performance of marine vessels and aircrafts is also limited by the friction force and has prompted interest in drag reduction methods using various active and passive techniques. Hitherto, polymer additives[1], near-wall injection of bubbles[2] and air layer[3] and wall surface modification[4–6] have been employed. The latter method of surface modification is of particular interest due to no requirement for a supply of polymer or pressurized gas and also the recent advances in micro/nano manufacturing techniques.

One of the latest surface modification techniques is the fabrication of micro/nano size patterns on an intrinsically hydrophobic material. The result is known as the superhydrophobic surface, in which the adhesion force cannot overcome the water surface tension because of the low surface energy of the material. This phenomenon is known as the Cassie state and results in a partially or fully non-wetted surface[7]. At this state, the micro-scale air pockets will be trapped and retain in the pores and voids of the surface forming a plastron. The slip of the liquid flow over this air plastron has the potential to result in a significant reduction of skin friction in both laminar and turbulent wall-bounded flows[6]. In terms of surface pattern, SHO surfaces have either ordered or random structures.

The SHO surfaces with ordered patterns are mostly fabricated through photolithography and soft lithography processes which require nanofabrication facilities and are typically limited to small surface areas (less than 100 cm^2). This has been ideal for experimental investigation of these surfaces for reduction of friction in small-scale laminar flows of microfluidic applications. The experiments of Ou *et al.*[8], Joseph *et al.*[9] and Byun *et al.*[10] and Choi and Kim[11] have confirmed significant slip velocity and reduction of skin friction in microchannels. Their results are in agreement with the general trend reported in the theoretical model of Lauga and Stone[12]. The quantitative agreement was obtained by Lee *et al.*[13] using surface structures performing close to the theoretical limits of wetting transition with significant slip length of 185 μm. Investigation of SHO surfaces with ordered patterns have also been extended to the turbulent regime showing the potential of skin-friction reduction and interaction with the turbulent structures.

In the turbulent regime, the recent experimental study of Park *et al.*[14] directly measured the skin-friction over a SHO with micro-scale grates using micro-flexure beams and showed up to 75 percent reduction of skin-friction. They also reported observation of plastron and its invariance once exposed to shear flow. Other investigations using PIV[15,16] or pressure drop measurements[15,17] on SHO with patterned structures have also shown about 9-30 percent reduction of skin-friction in low Re number turbulence. The numerical simulation of Min & Kim[18] showed reduction of skin-friction over a SHO surface represented with only streamwise slip and an increase of skin-friction over a SHO modeled with spanwise slip. These results have confirmed reduction of skin-friction using patterned SHO with nano or micro scale patterns with significant streamwise slip.

The investigation of the turbulent flow over SHO surface by the DNS of Min and Kim[18] has shown that the effect of SHO surface on the mean velocity profile is extended beyond the viscous sublayer to the buffer and the log layers. Martell *et al.*[19] showed in a DNS that mean velocity profile near the SHO wall scales with the wall shear stress and the log layer is offset by a slip velocity. The DNS of Jelly *et al.*[20] over SHO surface with streamwise micro-grooves has shown reduction of the strength of streamwise vortices and also the Reynolds shear stress. These numerical simulations have prescribed a slip boundary condition and obtained both a significant increase of mean velocity and a decrease in turbulent intensities over a wall normal distance extended to the logarithmic layer. However, the PIV experiment of Woolford *et al.*[21] on a SHO surface with patterned ribs and cavities in the range of 8-23 micron showed negligible change in the mean velocity profile and about 10 percent reduction of streamwise turbulent intensity. The PIV measurement of Daniello *et al.*[12] reports a large slip velocity of up to 40% of the mean channel velocity over micro-patterned SHO, however, no direct comparison is made with the mean velocity profile over a smooth surface. Further experimental investigation of the turbulent flow over a variety of surface patterns and Reynolds number is required to address the apparent discrepancy.

Despite the promising drag reduction with SHO surfaces with ordered pattern, their application is still constrained because of the complicated small-scale fabrication and low physical durability[22]. On the other hand, the SHO surfaces with a random texture have the advantage of large-scale fabrication through spray coating, spin coating or dip coating methods[23]. This

feature renders the random SHO surfaces viable for turbulent friction reduction over large surfaces of industrial applications. However, these are only a few experiments over SHO with random texture showing inconsistent trends. The experimental study of Zhao *et al.*[24] reported no appreciable decrease of skin-friction in turbulent flow over a flat plate with random SHO roughness. Later, Peguero and Breuer[25] conducted PIV measurements over two SHO surfaces with random patterns (sand-blast surface and random nanograss) and likewise did not observe any drag reduction in the turbulent regime. Aljallis *et al.* [26] carried out a drag measurement experiment on spray-coated SHO surface with random micro/nanoscale pattern over a wide range of Re number[26]. They showed 30% drag reduction in transitional flow (10^5<Re<10^6) but in high Reynolds turbulence (10^6<Re<10^7) drag increased. Aljallis *et al.* [26] speculated that the plastron depletion due to high shear flow resulted in a rough surface and increase of skin friction at high Re number. However, Gad-el-Hak[27] commented that the increase of skin-friction may not be due to the depletion of the air layer. The length scale of the surface roughness estimated from SEM photographs is lower than 1 μm, which implies the wetted surface is hydrodynamically smooth compared to the estimated thickness of the viscous sublayer (~15 μm). Most recently, Bidkar *et al.*[28] carried out a direct measurement of skin-friction on SHO surfaces with random texture of various surface characteristics using a floating plate assembly in Re number in the range of 10^6 to 9×10^7. Their results showed up to 30 percent reduction of skin-friction in fully turbulent flow prompting further investigation of the turbulent flow over large-scale SHO surfaces with random texture. Tian *et al.*[29] performed a PIV measurement on turbulent boundary layer flow over a SHO surface and observed approximately 10% drag reduction. Srinivasan *et al.*[30] reported 22% reduction in skin friction by spray deposition of SHO microstructures in a turbulent Taylor-Couette flow setup. The PIV measurement of Tian *et al.*[31] showed suppression of turbulent coherent structures due to the presence of a random SHO surface. Most recently, Zhang *et al.*[32] observed a maximum of 24% drag reduction and weaker vortical structures in a turbulent boundary layer over a random SHO. The apparent contradiction between the experimental results might be due to the depletion of the air pockets, relative size of surface textures to the flow scales (e.g., thickness of the viscous sublayer), and also measurement uncertainties.

Gad-el-Hak[27] has also emphasized on the necessity for detailed characterization of the turbulent flow over random SHO surfaces. In an effort to measure the mean flow and the turbulent

fluctuations over a hydrophobic surface with random pattern, Haibao *et al.*[33] performed hot-film anemometery. They reported that the turbulence intensity (bursting events intensity) and friction on hydrophobic surface (largest contact angle of 105.8°) are decreased compared to smooth wall flow. Their results are encouraging to further characterize the turbulent flow over superhydrophobic surfaces with a contact angle larger than 150° produced by a random surface texture. A detailed experimental investigation of the turbulent structure of the boundary layer can fulfill the shortcomings of numerical investigations in modeling the random surface pattern and shed light on the possible drag reduction mechanisms.

SHO coatings with random surface texture could have a higher longevity if produced with a hierarchical structure ranging from micro to nano-scale pores[22]. By employing such a coating on a rotating disc apparatus Moaven and Taeibi[34] achieved up to 15 percent drag reduction in the turbulent regime. Their results further suggested that drag reduction rate decreases with Re number. Bidkar *et al.*[28] also showed that reduction of skin-friction decreases with Re number for SHO surfaces with surface features comparable in size with the viscous sublayer. Therefore, a sustained drag reduction is obtained when the surface roughness is smaller than the viscous sublayer. However, these results are seemingly in contrast with the experiments of Daniello *et al.*[15]. Their measurements of mean velocity profile and pressure drop over a SHO surface with patterned micro-ridges demonstrated that the skin-friction reduction appears once the size of the surface features is comparable with the viscous sublayer thickness. Furthermore, they reported higher drag reduction at higher Re numbers with a thinner sublayer. The DNS of Martell *et al.*[19] also indicates that skin friction reduction increases with Reynolds number. This contradiction between surfaces with patterned and random structures might be attributed to the hierarchy of surface features on the random surface and their interference with the viscous sublayer. Precise measurement of turbulent statistics over both surface structures would help delineate the physics behind these dissimilar behaviors.

In view of the recent evidence regarding turbulent drag reduction of SHO surfaces with random surface texture, the present study aims to experimentally investigate the structure of the turbulent flow over these surfaces. The experiments are carried out in a large facility to provide a high spatial-resolution measurement system compared to the flow scales. Two PIV configurations with streamwise/wall-normal and streamwise/spanwise arrangements are applied

to comprehensively study the turbulent structure in terms of the mean flow, Reynolds stresses, higher-order turbulence statistics, and the length scale of the coherent motions. The measurements over the non-wetted SHO surface are compared with the wetted SHO counterpart (similar surface texture) and also a smooth surface. The experiments on the wetted SHO surface also demonstrate the behavior of a SHO surface upon complete depletion of the air layer.

II. EXPERIMENTAL SETUP

A. Flow facility

A closed-loop water channel at the Department of Mechanical Engineering of the University of Alberta is used for the current experiments. The water channel has a rectangular test section of 0.68 m wide, 0.47 m deep, and 5.2 m long made out of glass walls. The channel is operated at water depth of D = 420 mm in the current experiments. A flat-plate model with 3 m length made of cast acrylic with an elliptical leading edge and a sharp trailing-edge is placed parallel to the channel side-wall at a distance of W=50 mm to generate a channel flow as shown in figure 1. The measurements are carried out in this rather large facility to improve the measurement spatial resolution in comparison with the previous works[15,21]. The upper surface of the channel is also covered with an acrylic surface resulting in a rectangular channel with no free surface and an aspect ratio of D/W = 8.4. The measurement region is located 2 m (40W) downstream of the leading edge over a replaceable module, 50 cm long (x-direction) and 32 cm wide (z-direction), to incorporate the SHO (wetted and non-wetted) and smooth surfaces.

The experiments are carried out at an average velocity of U_b = 0.154 m/s corresponding to Re = 9,600 based on W. Two tripping wires are also installed 0.2m downstream of the leading edge to ensure a uniform transition to turbulence along the z-direction. The mean velocity profile is symmetric at the measurement region with maximum velocity of U_{max}= 0.177 m/s at the centerline (smooth walls on both sides).

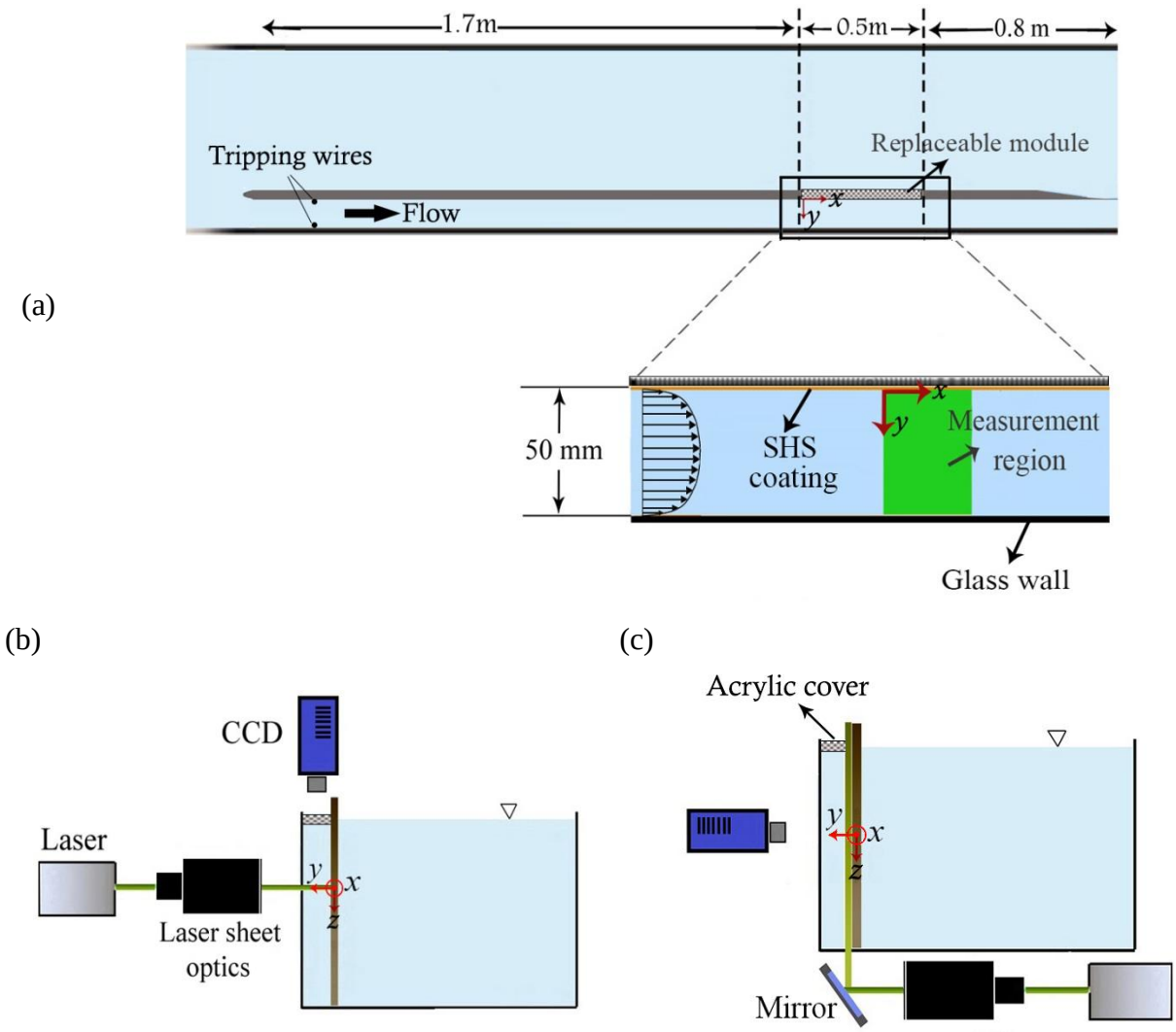

FIG. 1. A schematic view of the experimental setup showing (a) a top view of the channel flow formed between the flat-plat and the side wall of the water channel. (b) The arrangement of the camera and the illumination of the PIV system for the wall-normal/streamwise field-of-view and (c) the arrangement for the spanwise/streamwise field-of-view.

B. Fabrication and characterization of SHO samples

A random surface structure comprised of a hierarchy of micro and nano-particles was fabricated using spray coating (Ross Nanotechnology). The surface of the acrylic module was cleaned with ethanol to facilitate the adhesion of the SHO coating. An acrylic-based polymer solution was sprayed as a binding layer on the substrate followed by deposition of a mixture of micro and nano-particles in ethanol through a spray-coating procedure. After the solvent evaporates, the

micro-particles form the large roughness features of the surface as a porous matrix of approximately 30-50 μm thickness. The nano-particles stick to these structures and form a hierarchy to enhance the hydrophobicity as observed in figure 2. Figures 2.a-c represent the top-down scanning electron microscopy (SEM) images of the SHO surface. Figure 2.a with the lowest magnification (150X) gives an insight to the micro-scale roughness elements on the surface while figures 2.b (magnification of 2,500X) and 2.c (magnification of 10,000X) indicate the morphology of the roughness elements and the corresponding nano-particles covering surface which are in the order of 80 nm. Figures 2.d-f are images from a tilted angle of view providing an indication of the surface morphology. It is evident that the surface is completely covered with nano-particles. This hierarchical roughness in conjunction with the intrinsic hydrophobicity of the particles deters the water from wetting the solid surface. Therefore, air pockets are trapped in the micro/nano pores of the surface. To investigate the consequences of the depletion of the air pockets from the SHO surface, another SHO surface produced with similar procedure was wetted using an aqueous solution of a surfactant. The addition of the surfactant reduces water surface tension and results in a wetted surface. The wetted SHO surface is transparent both inside and outside of the water channel, which clearly distinguishes it from the non-wetted surface during the experiments. The contact angle (CA) of the non-wetted SHO is evaluated using the Krüss DSA 100 system (Krüss GmbH, Hamburg, Germany). Because of the very low surface energy of the SHO coating, the droplet did not detach from the dispenser needle showing a minimum CA of 165^{o}.

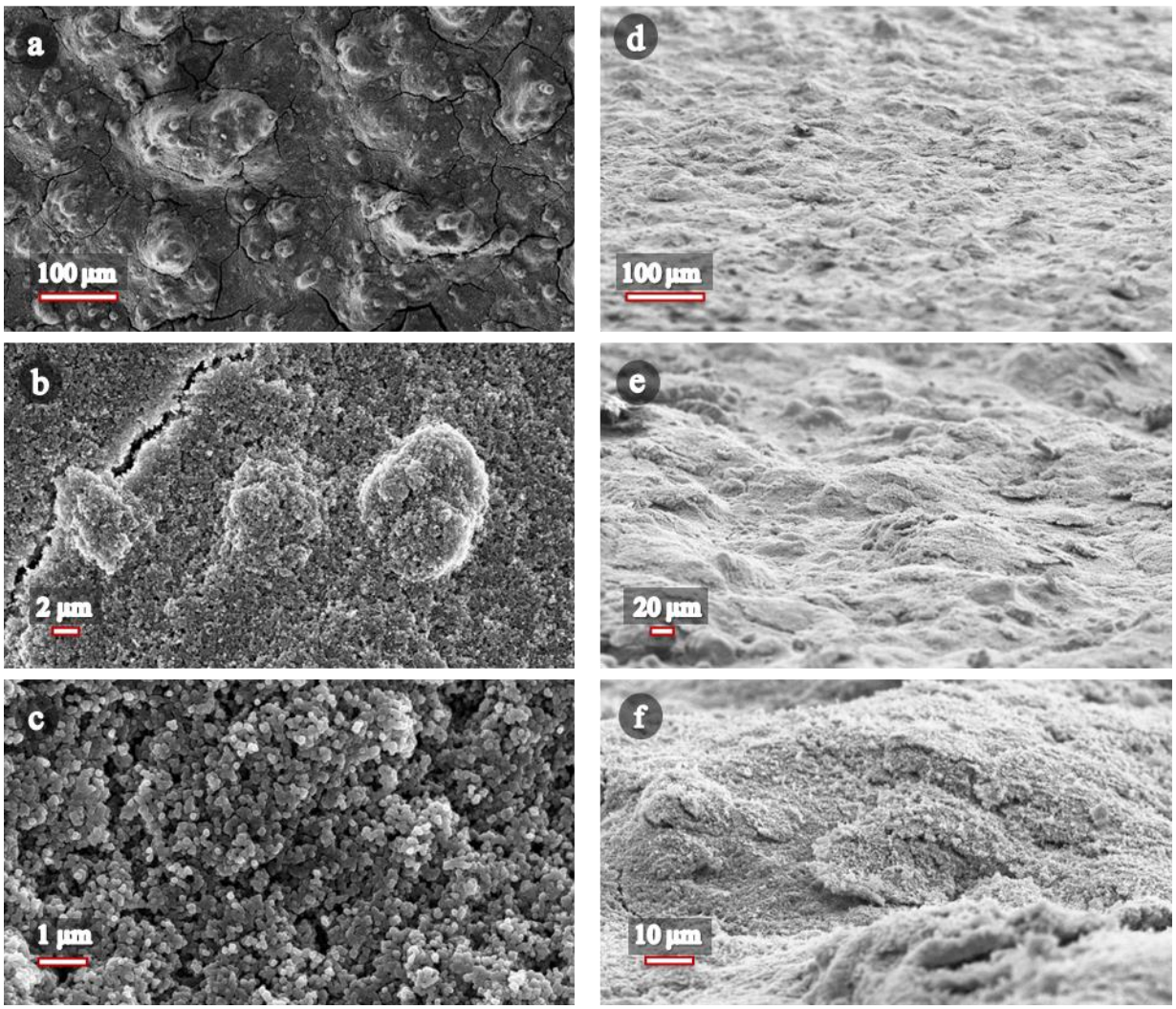

FIG. 2. SEM images of the SHO surface morphology at different magnifications. (a-c) are the top-down images and (d-f) represent the tilted angle of view. The SHO sample was fabricated on a 10 mm×10 mm microscope glass slide.

The profile of surface roughness of the SHO surface was measured using Ambios XP-300 surface profilometer with a resolution of 0.1 μm in wall normal direction. Five linear profiles were taken over a sampling length of 10 mm and the data were digitized at a sampling interval of 0.8 μm along the surface. A high-pass filter is applied to remove the inclination of the sample profile. Figure 3.a depicts a measured profile of the SHO surface. Three parameters are used to characterize the roughness profile (details in Appendix). The surface roughness R_a, also known as arithmetic roughness[35], is found to be 7.9 μm. The average root-mean-square height, R_{rms}, of the roughness profiles is 10.2 μm with a skewness of 0.66. The mean peak to trough roughness

height, R_{PT}, which is a representative of the equivalent sand-grain roughness[35], is 41 μm. The normalized form of these statistically calculated equivalent roughness measures are also illustrated in figure 3.a. k^+ is defined as $R_a u_{\tau 0}/\upsilon$, where $u_\tau = \sqrt{\tau_0/\rho}$ is the friction velocity, τ_0 is the shear stress on the smooth wall, ρ is the density, and υ is the kinematic viscosity of water. Therefore, based on all the roughness parameters shown in figure 3.a, the size of the surface features of the SHO surface used in the present work is almost one order of magnitude smaller than viscous sublayer thickness ($y^+=5$) in the current experiment. Therefore, if the air pockets are depleted the wetted surface is hydrodynamically smooth. Owing to the random nature of the current roughness, there might be sporadic wetted surface protrusions in contact with the liquid phase. This can be a drawback of the randomly-textured SHO surfaces which depending on the size of these protrusions reduces the friction reduction effect. For a wetted SHO surface, the roughness elements coming into direct contact with water flow increase the wetted area compared to the smooth surface. However, any changes to bulk flow depend on the relative roughness size to the flow length scale. Figure 3.b presents photographs of the wetted and non-wetted SHO surfaces submerged in still water. The wetted SHO surface is transparent while the non-wetted SHO is opaque due to the entrapped air pockets. The transparency of the wetted surface and the opaqueness of the non-wetted surface were maintained throughout the experiments while the surfaces were submerged under shear flow in the water channel. Recently, studies with similar SHO random roughness[30,36,37] have visualized the air plastron over the roughness features. Brennan *et al.*[36] used confocal microscopy to visualize and measure the thickness of the plastron over hydrophobized sand particles ranging from 50 to 710 μm in diameter (equivalent roughness characteristic is 84-700 μm) yielding a contact angle in the range of 130°. They observed 125-418 μm thick plastrons formed over the rather large-scale roughness present in quiescent water medium. The same group in another invetsigation[37], presented photos of plastron (obtained from confocal microscopy) over a soot-covered SHO surface with significantly smaller roughness size submerged in quiescent aqueous medium. The air fraction seems significantly higher compared with patterned surfaces (e.g., microridges). The most similar SHO sample to the surface of the current investigation in terms of roughness size is the surface produced by Srinivasan *et al.*[30] with roughness size of R_{rms}=8.5 μm and R_{PT}=35 μm. They have reconstructed 3D isosurface of the composite solid-air-liquid interface beneath a still water droplet deposited on the SHO revealing a higher air fraction compared with patterned

surfaces. Their measurements have shown a 12 μm slip length. However, all works with similar random roughness have carried out the plastron visualization in quiescent flow condition and to the author's knowledge there is no observation of the plastron thickness under high shear flows.

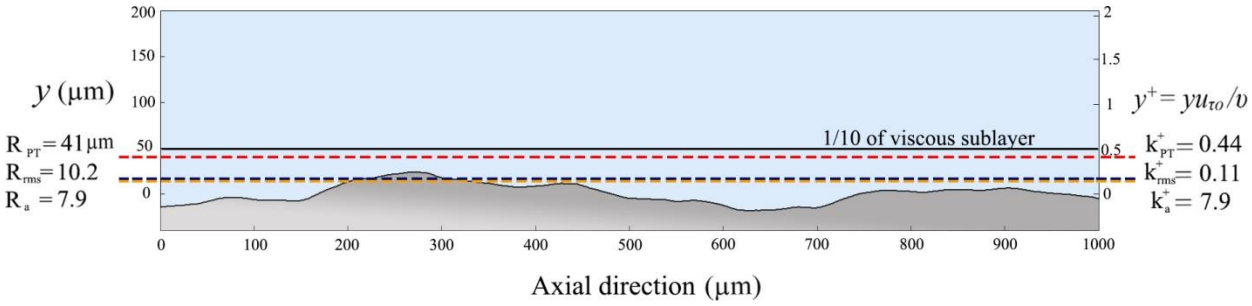

(a)

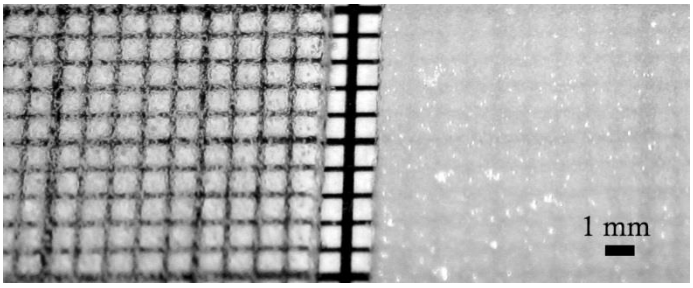

(b)

FIG. 3. a) The surface profile of SHO surface obtained from profilometery. The vertical axis on the left presents the roughness in μm while the dimensions normalized by inner scaling are shown on the right axis. Normalization is done by $u_{\tau 0}$ obtained from PIV experiments on the smooth surface. b) Photograph of the wetted (on the left) and non-wetted (on the right) SHO surfaces submerged in still water with a graph paper in the background. Light passes through the wetted SHO making the background grid visible, whereas for the non-wetted SHO the entrapped air pockets hinder the light passage.

C. Particle image velocimetry

Detailed characterization of the turbulent channel flow over the surfaces is carried out using two planar PIV configurations. The first field-of-view (FOV1) has a wall-normal/streamwise plane to capture the profile of mean velocity and the turbulent statistics in the wall-normal direction. The second field-of-view (FOV2) records spanwise/streamwise PIV images to scrutinize the low and high speed streaks within the inner layer. A schematic of both configurations is available in figures 1.b and 1.c.

The illumination for the PIV experiment was provided by a dual-cavity Nd-YAG laser (QUANTARAY PIV-400) with maximum output of 400 mJ/pulse and a wavelength of 532 nm. The laser has maximum operation frequency of 10 Hz and a pulse width of 5-8 ns. The laser initial beam diameter is 9 mm at the output which is collimated into a laser sheet of 30 mm wide and 1 mm thick. The water channel has been seeded with 12 μm hollow glass spheres (Potters Industries Sphericel® 110P8). A CCD camera with a sensor size of 2048×2048 pixel and 14 bit resolution (Imager ProX, LaVision) is applied to capture the images. Each pixel has 7.4 μm×7.4 μm area. A calibration target is used to establish the relation between the image coordinates and the physical space. The camera is equipped with a 105 mm SLR lens with an aperture setting of f / 5.6. For each data set 10,000 images were recorded with Δt = 1700 μs. Detailed information about the imaging system of the two PIV configurations is available in Table I.

The PIV images are improved for the cross-correlation algorithm by subtracting the ensemble minimum from the individual images. The images are further normalized by the ensemble average of the recordings. The mean velocity profile is obtained by averaging the cross-correlations over the ensemble of recordings[38,39]. This method increases the signal-to-noise ratio which allows a higher spatial resolution by allowing a smaller Gaussian interrogation window (IW) of 12×12 pixels with 75% overlap elongated with 4:1 aspect ratio in the streamwise direction. The instantaneous velocity fields for statistical investigation of the turbulent flow are obtained from cross-correlation of individual image pairs with IW of 48×48 pixels and 75% overlap. Similar processing algorithm with 48×48 pixels and 75% overlap was also applied to FOV2 images. The vector fields are post processed by universal outlier detection[40] and limiting the allowable vector range to -0.03 to +0.03 m/s for wall normal and 0 to 0.2 m/s for streamwise velocity. The removed spurious vectors are further interpolated and filled up. The PIV processing of all data sets are conducted in Davis 8.2 (LaVision, GmbH).

The relative in-plane spatial resolution of the PIV (i.e., window size) to the smallest length-scales of the turbulent flow can be used to assess the accuracy of the PIV system. In wall turbulence, Stanislas *et al.*[41] reported that the smallest coherent structures with a life time long enough to contribute to the turbulent statistics are approximately $20\lambda_0$. This length scale is equal to 1.71 mm in the current work (with λ_0=85.6 μm obtained from SOC PIV data) while the spatial resolution of the PIV is 1.24 mm. Saikrishnan *et al.*[42] applied a spatial filter on DNS data

to simulate the effect of finite window size on measurement of turbulent fluctuations using PIV. Their results show that a window size of 14λ (corresponding to current PIV measurement) captures about 96% of Reynolds stresses ($<u^2>$, $<v^2>$, and $<uv>$) in the buffer layer (y^+ =15) and 98% in the logarithmic region (y^+ =110). The underestimation reduced with increase of wall normal distance since the population of small scale turbulent fluctuations decreases. Therefore, the current PIV demonstrates sufficient spatial resolution to capture the turbulent statistics.

Table I. System specifications of the two planar PIV measurement configurations. The wall unit of λ_0 = 85.6 μm associated with the smooth surface is used to normalize the dimensions.

	FOV1		FOV2
Orientation	Wall-normal/streamwise		Spanwise/streamwise
Magnification	0.29		0.51
Digital resolution	38.6 pixel mm^{-1}		56.3 pixel mm^{-1}
Measurement field	2048 × 2048 pixels 53 mm × 53 mm $620^+ \times 620^+$		2048 × 2048 pixels 28.6 mm × 28.6 mm $333^+ \times 333^+$
Velocity vector	Individual correlation	Ensemble of correlations	Individual correlation
Interrogation window (IW)	48 × 48 pixels 1.24 mm × 1.24 mm $14.6^+ \times 14.6^+$	12 × 12 pixels 0.31 mm × 0.31 mm $3.6^+ \times 3.6^+$	48 × 48 pixels 0.85 mm × 0.85 mm $10^+ \times 10^+$
IW overlap	75 %	75 %	75 %
Vectors per field	170 × 170	680 × 680	134 × 134

III. RESULTS

A. Mean flow

The normalized mean flow velocity profiles across the channel with the smooth, non-wetted and wetted SHO surfaces are presented in figure 4.a. No considerable velocity difference is observed between the velocity profiles over the three surfaces. The mean velocity profile of the

wetted SHO is also very close to the smooth wall indicating that the surface is hydrodynamically smooth. The results are in contrast with the DNS of turbulent flow over SHO surfaces with patterned micro-ridge structures which are simulated using periodic no-slip no-shear boundary conditions[19,43]. Their results demonstrate about 30% increase in maximum velocity and a slip velocity in the order of 80% of bulk velocity. Nonetheless, the PIV experiments of Woolford *et al.*[21] over patterned SHO surface composed of micro-ridges (4 μm wide ridges with cavity width of 32 μm) also exhibited no appreciable near-wall difference in velocity profiles which is in agreement with the present measurements. Daniello *et al.*[15] reported a slip velocity about 40% of the mean velocity over SHO surface with micro-ridge pattern from PIV measurement. The relatively high slip velocity observed by Daniello et al[15] has been associated with the large streamwise grooves of 60 μm wide providing large shear free surfaces. Unfortunately, the velocity profiles are not compared with a smooth reference surface. There is also no information provided on the spatial resolution and measurement uncertainties of the applied PIV system. The discrepancy may also be due to the directionality of contact angle (or slip velocity) over a surface with streamwise micro-ridges in comparison with a random texture. Over a surface with streamwise micro-ridges, the streamwise slip is dominant over spanwise slip whereas for random texture SHO surface, slip is omnidirectional.

The magnified view of the normalized mean velocity profiles versus the wall normal distance normalized with the wall unit (λ_0=85.6 μm) is shown in figure 4.b. The profiles of the non-wetted SHO appear to have about 3-5% larger mean velocity within $4< y^+ < 15$ while the profiles of the smooth and the wetted surface overlap. The profiles also exhibit approximately identical wall shear stress which might be due to insufficient spatial resolution and measurement uncertainty of the PIV system within the sublayer ($y^+< 5$). In the immediate vicinity of the wall at $y^+< 4$, the velocity profile over the non-wetted SHO surface is smaller relative to the wetted surface. Our scrutiny of the PIV images shows that the sharp reduction of mean velocity at $y^+< 4$ is due to the biased error of PIV cross-correlation algorithm caused by the strong glare points at the non-wetted surface. The non-wetted SHO surface is covered with a thin air layer which renders a shiny irregular surface with high intensity glare points due to the change in refractive index. The reflections are much weaker in the case of smooth and wetted SHO as the laser light can pass through the surface due to transparency.

Measurement of slip length over superhydrophobic surfaces has been carried out previously in laminar micro-channels. Ou *et al.*[44] used micro-PIV and measured a 7.5 μm slip length for a patterned SHO surface in a laminar regime inside a micro-channel (channel width = 85 μm) using 1 μm fluorescent particles. Choi and Kim[11] reported a slip length of 20 μm over SHO surface with similar roughness as the current experiment using a cone-and-plate rheometer This would result in approximate slip-length of $0.2\lambda_0$ in current experiment. Srinivasan *et al.*[30] also carried out torque measurements in a turbulent Taylor-Couette flow with a SHO surface with roughness size (R_{rms}=8.5 μm) similar to current surface. Their results showed 12 μm slip length. The approximate value for the slip velocity over SHO surface is about 0.001 m/s (0.7% of the average channel velocity) by assuming a 12 μm slip length (similar to Srinivasan *et al.*[30]) and using the Navier's slip equation[6]. The accuracy of the current system is estimated about 0.0015 m/s (equivalent to 0.1 pix) for $y^+ > 10$. However, PIV uncertainty is even higher within the sublayer ($y^+ < 3$) due to higher velocity gradient, wall reflection, and non-uniform seeding.

Accurate measurement of slip velocity in the current experimental setup using micro-PIV is challenging due to the large scales of the facility and also limited spatial resolution of the measurement system. As it is detailed in section II.A, a channel width of W = 50 mm is considered here to optimize the system for measurement of turbulent structures within the inner layer. This resulted in a large wall unit (λ_0 = 85.6 μm) and consequently a larger the turbulent structures relative to the spatial resolution of the measurement system as also discussed in Section II.C. However, the large channel necessitates a long working distance for the imaging system (400 mm in the current work) and large amount of submicron flow tracers (potentially fluorescent) to seed about 5,000 liters of water.

The mean velocity profiles non-dimensionalized with inner scaling is also presented in semi-logarithmic scale in figure 5. As it is observed the measured mean velocity profile follows both law of the wall and the logarithmic law (κ= 0.41 and B=5.5). The Clauser method[41] is applied here to calculate the wall shear stress (τ_0 = 0.0874 N/m^2) and viscous length scale (λ_0=85.6 μm) of the smooth wall.

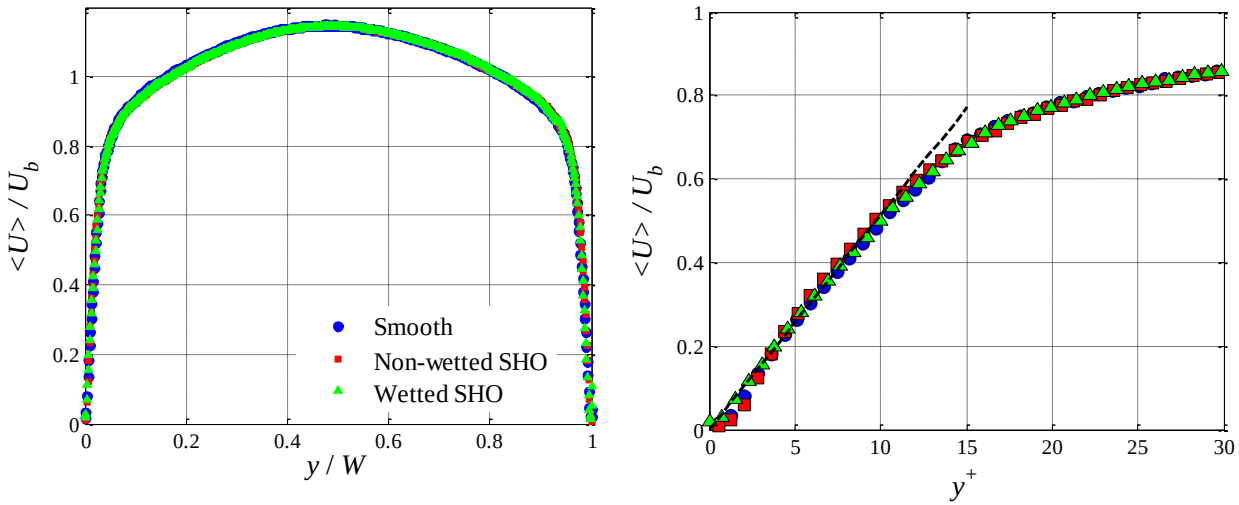

(a) (b)

FIG. 4. (a) Mean velocity profiles vs wall-normal distance normalized by outer scaling across the channel for the smooth, non-wetted and the wetted SHO surfaces, (b) Mean velocity profile in the inner-wall layer. The wall normal distance is normalized by inner scaling based on the reference value for wall shear stress obtained by Clauser method.

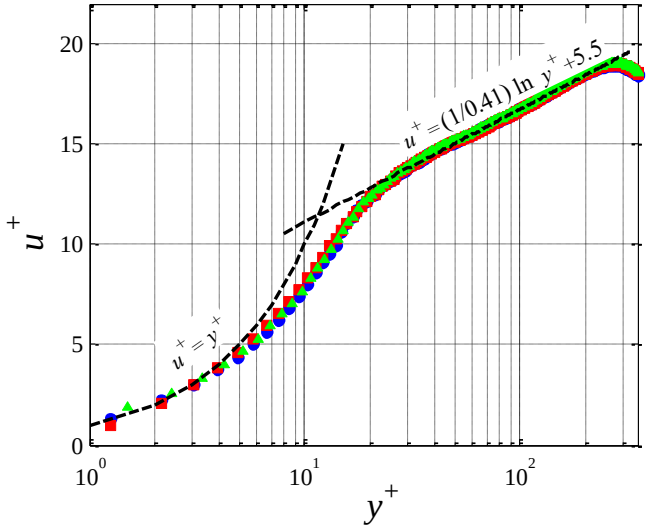

FIG. 5. The profiles of u^+ versus y^+. The wall normal distance is normalized by inner scaling based on the reference value for wall shear stress obtained by Clauser method. Labels are the same as figure 4.

The normalized profiles of streamwise Reynolds stress $<u^2>/u_{\tau 0}^2$ over the three surfaces are shown in figure 6.a. The erroneous data points at $y^+<10$ have been removed from the graphs in figure 6 to prevent ambiguity. Comparison of the smooth wall data of the current experiment at $Re_\tau = 246$ ($=\rho u_\tau W/\mu$) with the fully developed channel flow DNS of Moser *et al.*[45] at $\mathrm{Re}_\tau = 395$ shows similar trends. However, the peak values of the Reynolds stresses are slightly larger in comparison with the DNS data in which $<u^2>/u_{\tau 0}^2$, $<v^2>/u_{\tau 0}^2$, $<uv>/u_{\tau 0}^2$ approximately peak at

about 7.5, 1 and 0.75. The larger values are caused by the lack of a contraction section at the entrance of the channel and relatively short L/W as observed in figure 1. However, the relative magnitude of Reynolds stresses over the non-wetted SHO with respect to the smooth surface and wetted SHO is important and discussed here. The intensities of the smooth and the wetted SHO surface overlap which indicates that the micro-scale roughness of the wetted SHO surface (R_{PT} = 41 μm is one order of magnitude smaller than the viscous sublayer thickness) acts as hydrodynamically smooth wall with negligible effect on the turbulent flow[46]. It is also evident that the flow over the non-wetted SHO wall experiences lower streamwise turbulent fluctuations compared to the smooth and the wetted SHO surfaces. The non-wetted SHO surface exhibits about 12% attenuation in the peak value compared to smooth surface. Furthermore, the location of maximum $<u^2>/u_{\tau 0}^2$ for the non-wetted SHO is shifted about 3 wall units away from the wall demonstrating a thicker viscous sublayer. The wall-normal Reynolds normal stress $<v^2>/u_{\tau 0}^2$ profiles presented in figure 6.b also show a similar behavior with the profiles of smooth and wetted surfaces almost overlapping. The non-wetted SHO surface exhibits about 13% attenuation in the peak value compared to smooth surface. The maximum of $<v^2>/u_{\tau 0}^2$ is displaced away from the wall about 15 wall units. Normalized profiles of Reynolds shear stress $<uv>/u_{\tau 0}^2$ over the smooth and wetted SHO walls show negligible difference whilst it is smaller over the non-wetted SHO surface as observed in figure 6.c. The peak value reduces by 15 % and shifts about 15 wall units away from the wall for the non-wetted SHO surface. The reduction of Reynolds shear stress for flow over the current non-wetted SHO surface with random pattern demonstrates reduction of total shear stress due to the similar velocity profiles (similar viscous shear stress) and also reduction of turbulence production in the inner layer.

The distinguishable effects of the non-wetted SHO on the profiles of Reynolds stress were the variation in the intensity and the location of the maximum values. The current measurements show that the peak value of the Reynolds stresses attenuates and shifts away from the wall implying thicker viscous sublayer. This result is in agreement with PIV experiments of Tian *et al.*[31] in which, a SHO surface with similar roughness has been applied. They report that the Reynolds shear stress profile peaks at larger wall-normal distance for SHO surface. The PIV experiment of Woolford *et al.*[21] also shows attenuation of normal and shear Reynolds stresses with slight displacement of the peak value towards the wall over streamwise micro-ridges (streamwise slip). Their measurement over transverse micro-ridges (spanwise slip) shows an

opposite trend of intensification and displacement away from the wall. Similar trends as the experiment of Woolford *et al.*[21] is also observed in the DNS of Martell *et al.*[19,43] over patterned SHO surfaces. Their results showed that for streamwise micro-ridges the peak turbulence levels move towards the wall while in the case of transverse micro-ridges Reynolds stress profiles are similar to the smooth wall. Conversely, the DNS of Min and Kim[18] for flow over patterned surfaces with solely streamwise slip and combined streamwise-spanwise slip agrees with the current experimental observations. Their DNS simulation shows attenuation with the displacement of the peak location away from the wall for these two cases. However, for the case of only spanwise slip, $<u^2>$ intensifies and the peak location moves closer to the wall.

Figure 6 also demonstrates that the turbulence attenuations over the SHO surface are not limited to the sublayer and buffer layer and are well extended into the log layer with the highest variation at about $20 < y^+ < 50$ (buffer layer). Most of the turbulent activities occur in this region and have a growing dominance over the viscous effects. As y increases towards the channel center the profiles of the surfaces tend to merge. Hereafter, due the fact that wetted SHO surface acts as a hydrodynamically smooth surface the results associated with this surface will not be presented for brevity.

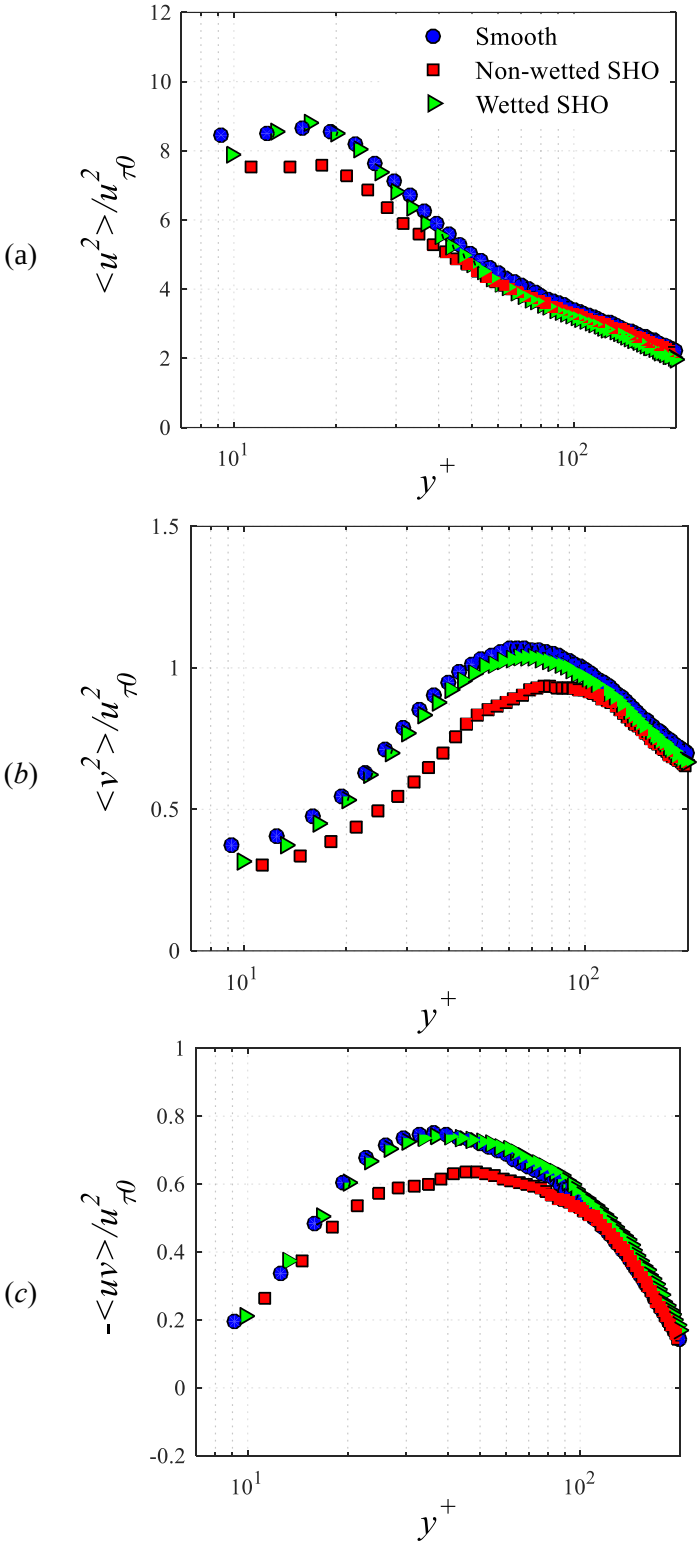

FIG. 6. Normalized profiles of normal Reynolds stresses (a) $<u^2>/u_{\tau 0}^2$ and (b) $<v^2>/u_{\tau 0}^2$ and the Reynolds shear stress (c) $-<uv>/u_{\tau 0}^2$ over the three surfaces.

B. Ejection and sweep events

Quadrant analysis is applied to scrutinize the effect of the non-wetted SHO surface on the turbulent motions in the near wall region. Figures 7.a-c show the quadrant distribution of u and v fluctuations on the smooth and the non-wetted SHO surfaces at $y^+ =$ 10, 20, and 30, respectively. The events responsible for the large negative Reynolds shear stress are the ejection ($u < 0$, $v > 0$) and sweep ($u > 0$, $v < 0$) motions over both surfaces. In a turbulent wall flow, the ejections have a larger contribution to the Reynolds shear stress across most of the wall normal distance. The contribution of the ejections reduce with moving closer to the wall as the sweep events become more pronounced with larger contribution to turbulence production in the sublayer[47]. This trend is clearly observed in figure 7.a-c as the u-v distribution become more skewed towards the ejection events (higher probability on the left side of $u = 0$ axis) with increase of y^+ over the smooth surface.

The sweep events over the non-wetted surface are observed to be weaker in comparison with the sweeps of the smooth surface. This is evident from the smaller area covered by the 0.1% contour of the non-wetted SHO surface at the fourth quadrant (Q_4) of figure 7.a. The ejection events have a similar strength for both surfaces as the contours almost overlap in the second quadrant (Q_2) of figure 7.a. In figure 7.b, there is slight increase of the strength of sweep events over the non-wetted SHO in the Q_4 quadrants. As the wall normal distance increases, the difference in the contours at Q_4 quadrant (sweep) decreases and discrepancy of the contours is related to the Q_2 quadrant (ejection) as observed in figure 7.c. This implies that in the sublayer the non-wetted SHO surface attenuates the sweep events while outside of the sublayer in the buffer layer the effect on the sweep events weakens and the ejection events are attenuated. Therefore, the maximum reduction of Reynolds shear stress which was observed in figure 6.c at $y^+ = 30$ is due to the dampening of the ejection events.

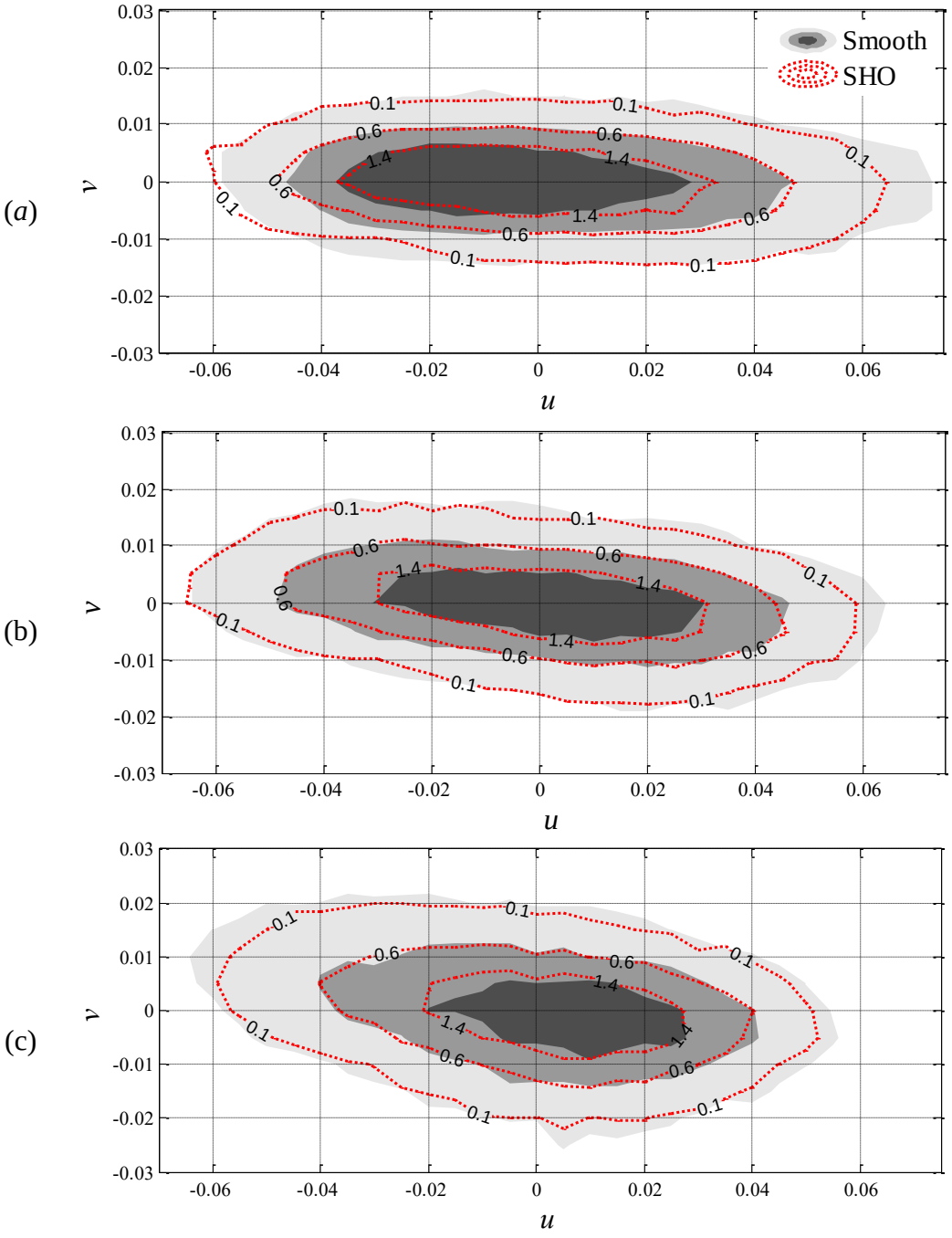

FIG. 7. The probability density function (PDF) of turbulent motions over the *u*-*v* quadrant within the boundary layer at wall-normal locations of (a) $y^+ = 10$, (b) $y^+ = 20$, (c) $y^+ = 30$. The filled contours illustrate the PDF velocity fluctuations over the smooth surface while the red dotted contours represent the non-wetted SHO surface. The dark gray, medium gray and light gray colors denote 1.4, 0.6 and 0.1 % PDF values. The PDFs are in percentage and the velocity fluctuations are in m/s.

Conditional averaging of Reynolds shear stress based on the four quadrants provides detailed information on the contribution of ejection and sweep motions to the total turbulence

production. The results are presented in figure 8 for the non-wetted SHO and the smooth surface. The profiles associated with Q_2 and Q_4 events (figure 8.a) contribute to positive turbulence production (negative Reynolds shear stress) and the profiles associated with Q_1 and Q_3 events (figure 8.b) contribute to negative turbulence production (positive Reynolds shear stress)[48]. For both the smooth and non-wetted SHO surfaces, the conditional average of the Q_4 events is larger than the Q_2 events near the wall at $y^+<15$. Consequently, the Q_4 events (sweeps) dominate at the near-wall region ($y^+<15$) which is in agreement with Kim *et al.*[48] DNS simulation of turbulent channel flow [48]. As the distance increases the Q_2 events dominate the turbulence production. This overall trend of sweep and ejection dominance is similar for both the smooth and non-wetted surfaces. However, a suppression of both the ejection and sweep events is observed over the non-wetted SHO surface corroborating the experimental results of Haibao *et al.*[33] and Tian *et al.* [29] and DNS simulations of Jelly *et al.*[20]. Compared to smooth wall, the peak activity of Q_2 and Q_4 events over the SHO surface is suppressed by 15% and 17%, respectively. Jelly *et al.*[20] reported 23% and 17% reduction of Q_2 and Q_4 values for flow over SHO surface comprised of streamwise ridges. A difference between the present results and the DNS simulation of Jelly *et al.*[20] is in the wall normal displacement of the peak values. According to figure 8.a, the wall-normal positions of peaks have moved away from the wall which is consistent with the turbulent intensity profiles of figure 6. However Jelly *et al.*[20] reported an opposite displacement of the peak locations. The conditional average of Q_1 and Q_3 events in figure 8.b also reduce over the non-wetted SHO wall agreeing with Jelly *et al.*'s results except for the near wall region where they report a bulge in Q_1 magnitude. They associated it to a region of negative turbulent kinetic energy production. On the whole, both the sweep and ejection events are suppressed over the non-wetted SHO surface leading to smaller Reynolds shear stress and consequently attenuation of turbulence production. As a result, theoretically skin-friction would decrease over a non-wetted SHO surface.

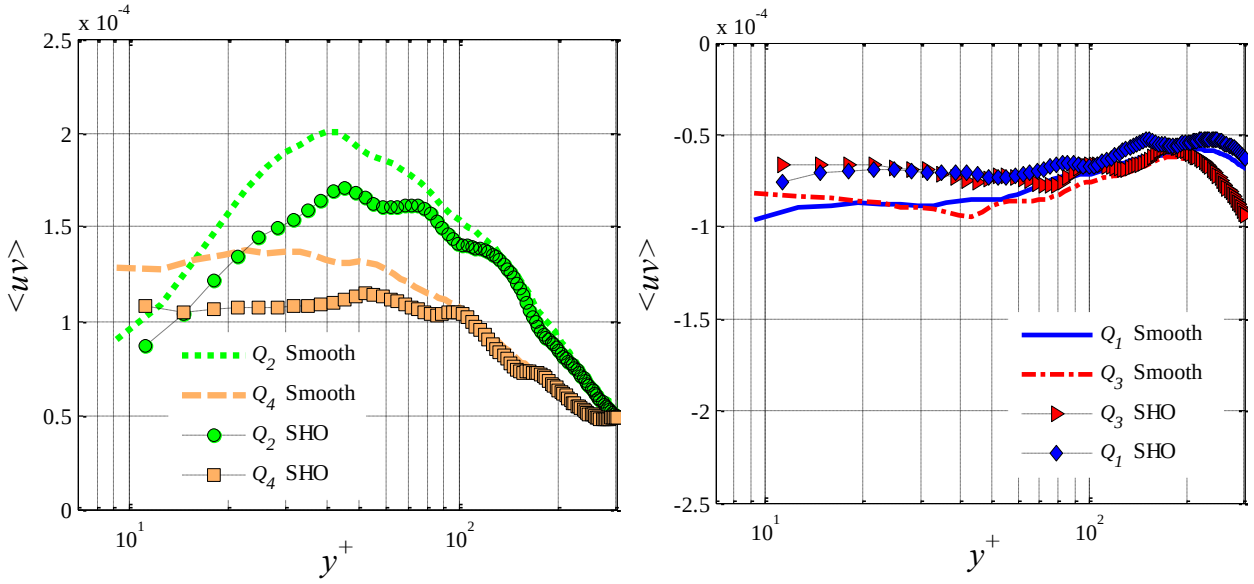

(a) (b)

FIG. 8. Contribution of (a) second and fourth quadrants, (b) first and third quadrants to Reynolds shear stress $<uv>$ (m^2/s^2).

The triple products of the turbulent fluctuations are investigated to identify the direction of the transport of turbulent kinetic energy. The experiments of Andreopoulos and Bradshaw[49] on turbulent boundary layer over a rough wall indicated that the triple products of velocity fluctuations can reveal the changes in turbulence structures induced by surface boundary condition. There is no significant change in the general trend of turbulent structures and transport in triple products on figure 9 over the smooth and the non-wetted surfaces. The transport direction of $<u^2>$ component of the turbulent kinetic energy (TKE) by means of streamwise velocity fluctuations is indicated by $<u^3>/u_{\tau 0}^3$. The positive value of $<u^3>/u_{\tau 0}^3$ observed in figure 9.a confirms the dominance of the sweep events (fourth quadrant) at $y^+ < 12$ while the negative values beyond $y^+ > 12$ show the weakening of the sweeps and the growing dominance of the ejection events (second quadrant) in transport of $<u^2>$ over both surfaces. However, a noticeable attenuation of $<u^3>/u_{\tau 0}^3$ is observed over the non-wetted SHO surface in the range of $15 < y^+ < 50$.

Figure 9.b shows the distribution of $<v^3>/u_{\tau 0}^3$ which represents wall-normal transport of the $<v^2>$ component of TKE by means of wall-normal velocity fluctuations. The direction of $<v^2>$ TKE transport is towards the wall within $8 < y^+ < 33$ and away from the wall for $y^+ > 33$. Similar

to $<u^3>/u_{\tau 0}^3$ results, the intensity of these wall-normal motions is significantly decreased over the non-wetted SHO wall.

Figure 9.c demonstrates the velocity triple product $<u^2v>/u_{\tau 0}^3$ which indicates the wall-normal transport of $<u^2>$ by means of wall-normal velocity fluctuation (v). The negative sign of $<u^2v>/u_{\tau 0}^3$ at $y^+<15$ implies transport of $<u^2>$ towards the wall for both smooth and SHO surfaces. For $y^+>15$, the turbulent transport of $<u^2>$ is directed away from the wall as the sign of $<u^2v>/u_{\tau 0}^3$ is positive. The streamwise transport of $<v^2>$ stress presented by $<uv^2>/u_{\tau 0}^3$ is shown in figure 9.d. The positive values for smooth and SHO profiles adjacent to the surface ($y^+<19$) suggests that streamwise acceleration of the streamwise transport of Reynolds stress has been attenuated. Away from the wall ($y^+>19$), streamwise deceleration of transport of Reynolds stress is also reduced implying that regardless of acceleration or deceleration in streamwise transport presence of SHO surface reduces the turbulent fluctuations. The streamwsie and wall-normal turbulent flux of u^2 and v^2 contribution to TKE have been declined for flow over the non-wetted SHO wall compared to reference smooth wall regardless of the transport direction resulting in turbulent production deficit.

Although the quadrant analysis provides helpful information on the contribution of ejection and sweeps to the turbulence production, it does not reveal the properties of vortical structures associated with these motions. Further analysis on the length scales and vortex structures would shed light on the effect of surface slip on turbulent flow structures.

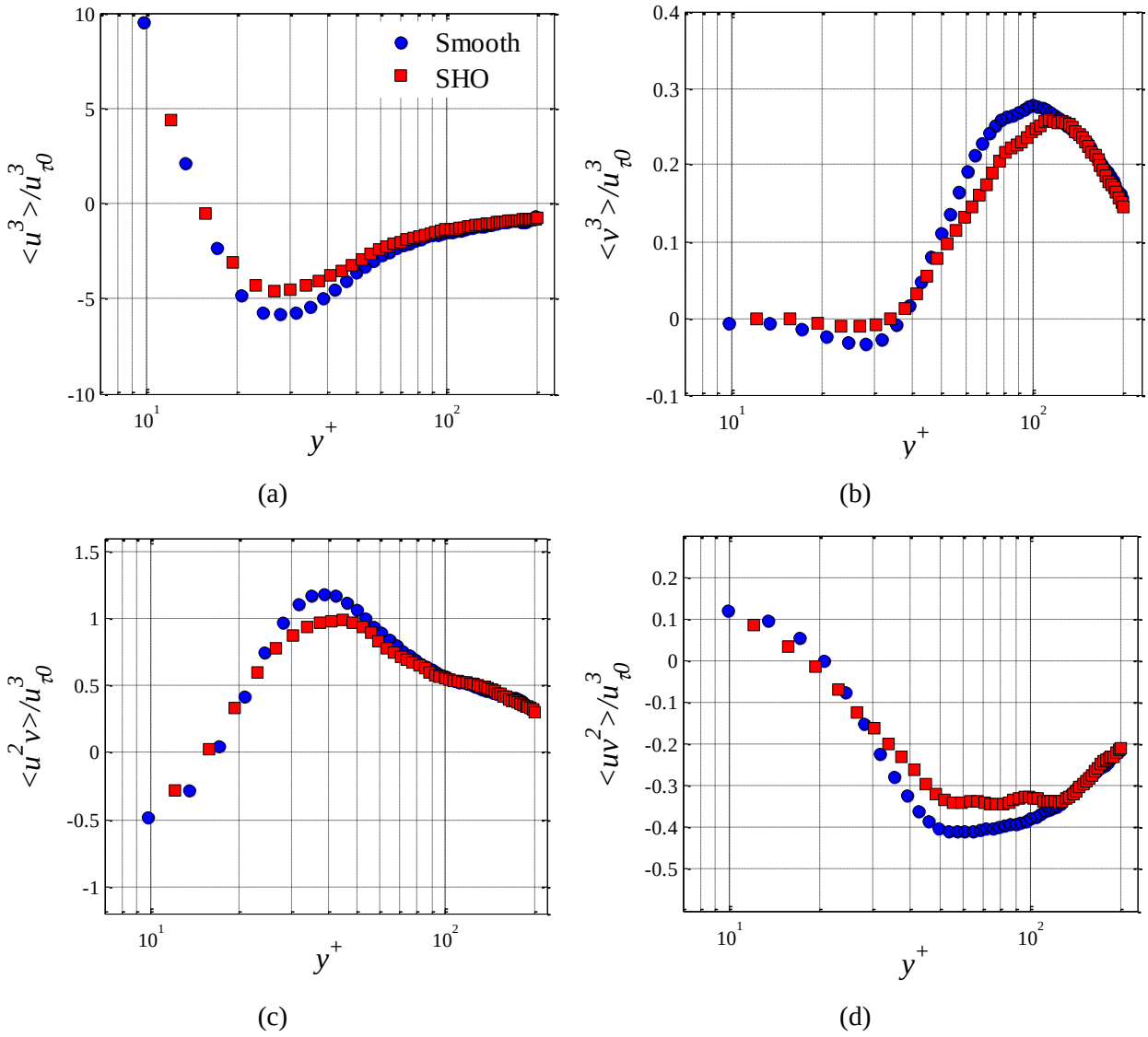

FIG. 9. The velocity triple products for the smooth and the non-wetted SHO surfaces in inner scaling (a) $<u^3>/u_{\tau 0}^3$, (b) $<v^3>/u_{\tau 0}^3$, (c) $<u^2v>/u_{\tau 0}^3$, (d) $<uv^2>/u_{\tau 0}^3$.

C. Length scales

Characterization of the turbulence structures especially in the near-wall can elucidate the mechanism of skin friction reduction. In a turbulent boundary layer, the streamwise and quasi-streamwise vortices strongly interact with the low and high speed streaks through ejection and sweep motions. According to White *et al.*[50], there is a consensus that regardless of the drag reduction method, the effect of various drag reduction methods includes weakening of the streamwise vortices which results in decrease of the strength and increase of the spanwise

spacing of the streaks [1,2,18]. The spanwise spacing of the streaks is characterized using spanwise correlation of streamwise velocity fluctuations,

$$C_{uu} = \frac{\langle u(y_0,z)u(y_0,z+\Delta z)\rangle}{\langle u(y_0,z)^2\rangle} \quad (1)$$

where y_0 is the wall-normal distance. The C_{uu} values associated with the spanwise spacing of the near-wall low-speed streaks at y_0^+=14 are presented in figure 10.a for the smooth and the non-wetted surfaces. The streak spacing is defined as twice the spanwise Δz for the minimum value of C_{uu}[50,51]. The minimum of C_{uu} occurs at Δz^+= 64 and Δz^+=71.2 for smooth and non-wetted SHO surfaces, respectively. The separation of around 128λ_0 (Δz^+= 64.0) for the smooth surface is consistent with White *et al.*[50] at the same y^+. The spanwise spacing over the non-wetted surface increases by 11% (14λ_0) demonstrating thicker streaky structures and reduction of turbulent production in the near wall region. Tian *et al.*[31] have reported similar behavior for spanwise spacing of the low-speed streaks. The interface of the low and high speed streaks is known to be populated with quasi-streamwise vortices[47,52]. This relatively lower density of streaks theoretically lowers the population density of the vortices leading to skin friction reduction which is also in agreement with the simulation of Jelly *et al.*[20].

The streamwise correlation of streamwise velocity fluctuations following

$$C'_{uu} = \frac{\langle u(x,y_0)u(x+\Delta x,y_0)\rangle}{\langle u(x,y_0)^2\rangle} \quad (2)$$

obtained at Δx^+= 240 is plotted versus the wall normal distance (y_0) to characterize the streamwise length scales of the flow structures. As shown in figure 10.b, in the range of 10< y^+ <40 which mostly covers the buffer layer, the flow structures have been attenuated in size implying the dampening of the ejection events. In this y^+ range, the dominant flow structures are the streamwise vortices. Weakening of the ejection events could in turn lead to weaker streamwise vortices that are responsible for high turbulent fluctuations and consequently high skin-friction. The reduction in the average streamwise length scale of the structures over the non-wetted SHO surface further continues for y^+ > 50 also shows that the large scale flow structures of the logarithmic and the outer later are also attenuated over the non-wetted SHO surface.

(a)

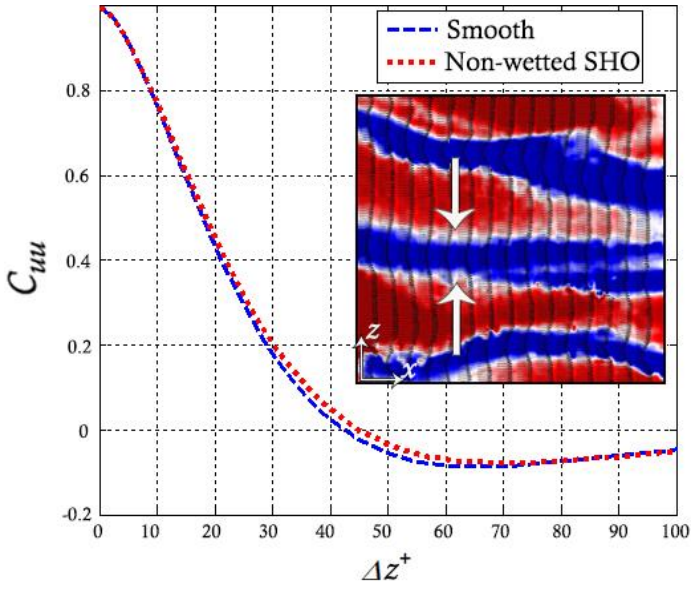

(b)

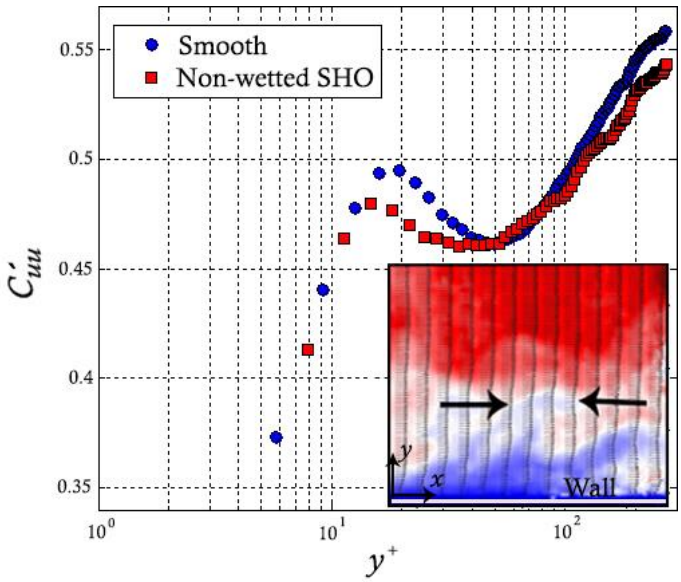

FIG. 10. (a) Spanwise correlation function of the streamwise velocity in *x*-*z* plane at y^+=15. The image presents the vector field from streamwise/spanwise FOV2 (*x*-*z* plane) and the arrows show the spanwise thickness of the low speed streak. (b) Streamwise correlation values of the streamwise velocity at *x*-*y* plane corresponding to Δx^+= 240. The image presents the vector field from streamwise/wall-normal FOV1 (*x*-*y* plane) and the arrows show the streamwise size of the sample flow structure.

D. Vortex analysis

The strength of vortical structures provides an indication of turbulence production within near wall region. The *Q*-criterion proposed by Hunt *et al.*[53] is applied to identify and evaluate the vortical structures. Figure 11.a presents the conditional average of the *Q* values over regions with $Q > 0.5Q_{max}$ where Q_{max} corresponds to maximum Q over the ensemble of data. The *Q* values are obtained from planar PIV data (FOV1) associated with the structures in the *x*-*y* plane. This conditional averaging only selects vortex cores with large rotation over strain ratio. Relative to the reference smooth surface, vortex strength over the non-wetted SHO surface has been decreased by 12% in the buffer layer. The difference is mostly apparent in the near-wall region (buffer layer) and it diminishes with increase of wall-normal distance. In the outer layer at $y^+ > 50$, due to the lower population of the strong vortices, the conditional average does not reach statistical converge. In the near-wall region, the spanwise-oriented vortices are associated with the early stages of hairpin vortex growth or tilted quasi-streamwise vortices[54]. The results confirm reduction in C'_{uu} values in buffer region over the non-wetted surface (figure 10.b), both implying weakening of the vortical structures in spanwise direction. These vortical structures induce sweep and ejection events which contribute to the Re stress production[20]. Also reflected in quadrant analysis, weakening of the vortical structures leads to suppression of the sweep and ejection events which in turn decreases Re shear stress contribution to the skin friction. Figure 11.b further supports the idea of weakening of the vortices over SHO surface. This figure illustrates that the area covered by the spanwise vortical structures detected using $Q > 0.5Q_{max}$ threshold and normalized by the total area of FOV1. The results show reduction of the fractional area over the non-wetted SHO surface in the buffer layer. Figures 11.a and b indicate weakening of the vortical structures in strength and size and therefore reduction of turbulence production. These results are in agreement with DNS of Jelly *et al.*[20] as well as the PIV measurement of Tian *et al.*[31] who reported vortex packets with smaller length scales.

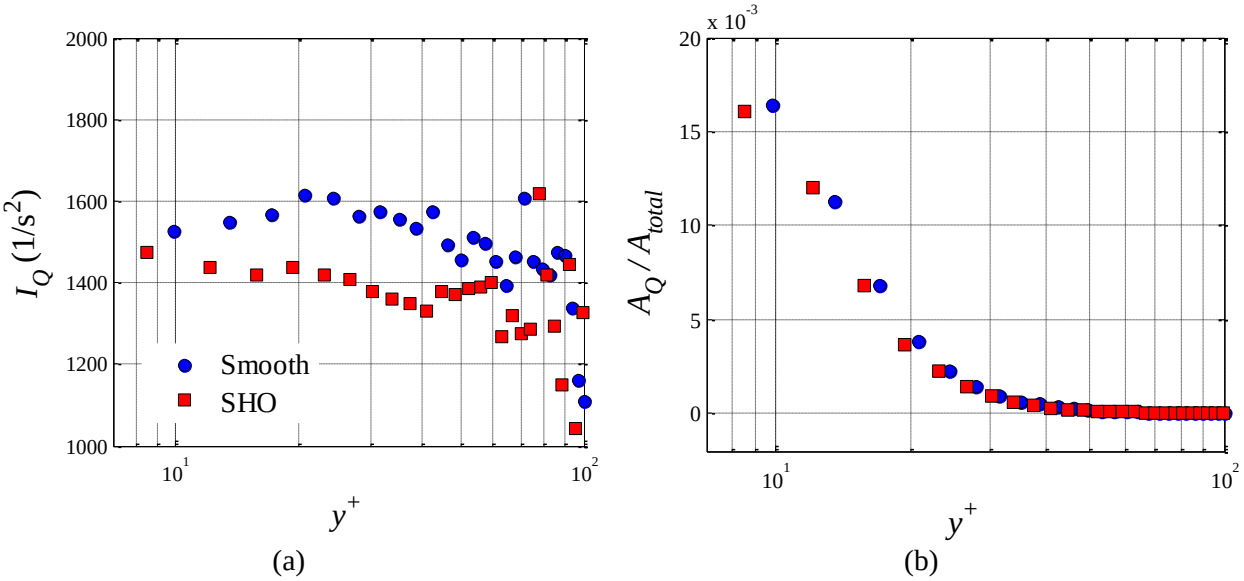

FIG. 11. (a) Conditional average of regions with $Q > 0.5Q_{max}$ associated with the spanwise vortex strength versus wall-normal direction. (b) Normalized area of vortical structures detected according to $Q > 0.5Q_{max}$.

IV. DISCUSSION

A significant reduction of the Reynolds normal and shear stresses (10-15 percent) was observed over the non-wetted SHO surface in the wall-normal range of $10 < y^+ < 100$. The mean velocity profile also shows a small increase of about 3-5 percent over $5 < y^+ < 15$. A negligible variation of mean velocity profile accompanied by about 10% variation of Reynolds stress is also observed in the PIV measurement of Woolford *et al.*[55] over a sample with L/W of 27. However, the DNS of Martell *et al.*[19] reports about 25% increase in maximum velocity values and more than 50% reduction in wall shear stress. In general, the mean velocity profile is not expected to vary in the same order of magnitude as the Reynolds stresses. For example, about 10% change of mean velocity profile (normalized by average channel velocity) corresponds to about 20% change in Reynolds shear stress due to change of channel Re number from 5,600 to 13,750 in the DNS of Kim *et al.*[36]. However, the variation of the mean velocity profiles in the experiments appears relatively small and over a limited range of y^+ in comparison with the results of DNS. The smaller variation in the mean velocity profile over the SHO surface in this work might be associated with the short length of the SHO sample ($8W$) which does not provide sufficient length for the mean velocity profile to adapt to the new surface boundary condition and reach an equilibrium state.

The orientation of the slip velocity over a SHO surface also affects the attenuation or intensification of the turbulent fluctuations. The flow over ordered SHO surfaces with streamwise grooves experiences dominance of streamwise slip while the spanwise grooves work vice versa[55]. Nevertheless, over a SHO surface with random texture, the slip would be omnidirectional and the flow would experience slip in both streamwise and spanwise directions. According to the DNS results of Min and Kim[18], turbulent flow over a surface with omnidirectional slip boundary condition experiences lower rates of drag reduction compared to a surface with merely streamwise slip velocity. This has been attributed to the intensification of streamwise vortices due to the spanwise slip component. Therefore, on a random texture SHO, the attenuation of the streamwise vortices due to streamwise slip is opposed by the adverse effect of spanwise slip. This adverse effect has resulted in 6% increase in the value of $\langle w^2 \rangle$ over the non-wetted SHO wall at $y^+=15$ based on FOV2 measurement. This implies that despite the favorable effect of decreasing $\langle u^2 \rangle$ and $\langle v^2 \rangle$, spanwise slip of the randomly-textured SHO increases the spanwise turbulent fluctuations which may also oppose the near-wall variation of mean velocity.

The streamwise slip velocity resulted in larger streak spacing as it was observed in figure 10.a. The streaks are also more coherent and consequently their population density reduces similar to the observations of other drag reduction methods[1,2,18]. The steamwise low and high speed streaks are generated by the streamwise vortices of the inner layer[52], therefore, the streamwise vortices are also attenuated in number density and strength. The results show an increase in spacing and consequently reduction in number of streaks, and accordingly the number of streamwise vortices is also predicted to decrease. This trend is also reported in the DNS of Jelly *et al.*[20] in which a remarkable decrease in the population density of the vortices is observed. A reduction in the strength and size of the spanwise vortices is also observed in figure 11. The suppression of the vortices attenuated the ejection and sweep motions as it was evident in figures 7-9. Smaller streamwise flow structures in figure 10.b further supports the idea that SHO surface suppresses the turbulence generation by weakening the ejection/sweep motions and reducing their interaction with the mean shear. Therefore, the turbulence production and subsequently skin-friction reduces. However, as discussed above the spanwise slip may adversely affect the drag reduction process by amplifying spanwise fluctuation and increasing the spanwise turbulent intensities.

The reduction of Reynolds stresses suggests that SHO surfaces with random patterns can lead to skin-friction drag reduction in a channel flow. This conclusion is consistent with the experiments of Bidkar *et al.* [28] demonstrating that to achieve for skin friction reduction, the roughness size of the SHO texture should be one order of magnitude smaller than the thickness of the viscous sublayer. This criterion also applies to the current experiment as observed in figure 3.a. The current results also supports Gad-el-Hak's[27] comment regarding measurement uncertainties of the possibly wetted SHO surface in the work of Aljallis *et al.*[26]. According to the discussion of Bidkar *et al.*[28], the roughness size becomes comparable with sublayer thickness in higher Reynolds numbers and the drag reduction decreases. Furthermore, current experiments showed that the wetted SHO surface is hydrodynamically smooth and does not increase skin friction. Therefore, the drag increase in Aljallis *et al.*[26], which was initially speculated to be due to the adverse effect of wetting, might be associated with the measurement uncertainties or the uncontrolled experimental conditions including changes in the location of laminar-turbulent transition due to vibration and superhydrophobicity as explained by Gad-el-Hak[27].

V. CONCLUSION

Turbulent flow over smooth, non-wetted SHO and wetted SHO surfaces is experimentally investigated. Flow characteristics are measured using planar PIV applied in two different configurations of streamwise/wall-normal and streamwise/spanwise planes. The features of the SHO surface are at least an order of magnitude smaller than the sublayer thickness. A small increase in mean velocity (3-5%) is observed within $4 < y^+ < 15$ over the non-wetted SHO surface. The normal and shear Reynolds stresses attenuate in the buffer and logarithmic layers by 15% with the peak wall-normal position moving away from the wall by 15 wall units. The flow over the wetted SHO surface does not experience any change in the mean velocity nor in the Reynolds stresses. This agrees with that fact that the roughness size is smaller than the thickness of viscous sublayer rendering a hydrodynamically smooth wall. Quadrant analysis of the sweep and ejection events suggests that the sweep/ejection events are suppressed due to the slip on the non-wetted SHO surface. The non-wetted SHO surface tends to have a stronger effect on the ejection events with increase of wall-normal distance. The intensity of the ejection and sweep events over the SHO surface is suppressed by 15% and 17% in comparison with the

smooth wall, respectively. It was also seen that the transport of the turbulent kinetic energy is attenuated. The streamwise low and high speed streaks over the non-wetted SHO surface evolve to more coherent structures with 11% increase in spanwise spacing. Analysis of vortical structures showed that the string spanwise vortical structures attenuate by 13% in the buffer layer over the non-wetted SHO. The reduction of Reynolds stresses along with attenuation of the ejection and sweep motions, low and high speed streams and the vortical structures indicate lower turbulence production over the non-wetted SHO surface.

ACKNOWLEDGMENTS

This work has been partially supported by the Natural Sciences and Engineering Research Council of Canada (NSERC RGPIN 1512 GHAEMI). Authors also acknowledge Sina Rafati for further evaluation of the results using PTV analysis.

APPENDIX

APPENDIX: SURFACE ROUGHNESS PARAMETERS

The surface roughness R_a, also known as arithmetic roughness [35], is defined as:

$$R_a = \frac{1}{L}\int_0^L |Z(x) - \bar{Z}|\, dx \tag{A1}$$

where $Z(x)$ is the wall-normal coordinate of the surface, L is the profile measurement length and $\bar{Z}$ is the mean of the measured profile Z(x).

The average root-mean-square height, R_{rms}, of the roughness profiles is found from

$$R_{rms} = \sqrt{\frac{1}{L}\int_0^L |Z(x) - \bar{Z}|^2\, dx} \tag{A2}$$

The mean peak-to-trough roughness height is defined as the average of the maximum peak-to-trough heights of roughness profiles within five consecutive sampling subsections of the measured profiles[35]

$$R_{PT} = \frac{1}{5}(Z_1 + Z_2 + Z_3 + Z_4 + Z_5) \tag{A3}$$

where Z_i is the maximum peak-to-trough height in i-th sampling subsection length.

The skewness of the profile is defined as:

$$Skewness = \frac{1}{R_{rms}^3}\left[\frac{1}{L}\int_0^L |Z(x) - \bar{Z}|^3\, dx\right] \quad \text{(A4)}$$

REFERENCES

1 White, C. M. & Mungal, M. G. Mechanics and Prediction of Turbulent Drag Reduction with Polymer Additives. *Annu. Rev. Fluid Mech.* **40,** 235–256 (2008).

2 Sanders, W. C., Winkel, E. S., Dowling, D. R., Perlin, M. & Ceccio, S. L. Bubble friction drag reduction in a high-Reynolds-number flat-plate turbulent boundary layer. *J. Fluid Mech.* **552,** 353 (2006).

3 Elbing, B. R., Winkel, E. S., Lay, K., Ceccio, S. L., Dowling, D. R. & Perlin, M. Bubble-induced skin-friction drag reduction and the abrupt transition to air-layer drag reduction. *J. Fluid Mech.* **612,** 201–236 (2008).

4 Choi, K. The rough with the smooth. *Nature* **440,** 754 (2006).

5 Carpenter, P. The right sort of roughness. *Nature* **388,** 713–714 (1997).

6 Rothstein, J. P. Slip on Superhydrophobic Surfaces. *Annu. Rev. Fluid Mech.* **42,** 89–109 (2010).

7 Lafuma, A. & Quéré, D. Superhydrophobic states. *Nat. Mater.* **2,** 457–60 (2003).

8 Ou, J., Perot, B. & Rothstein, J. P. Laminar drag reduction in microchannels using ultrahydrophobic surfaces. *Phys. Fluids* **16,** 4635–4643 (2004).

9 Joseph, P., Cottin-Bizonne, C., Benoît, J. M., Ybert, C., Journet, C., Tabeling, P. & Bocquet, L. Slippage of water past superhydrophobic carbon nanotube forests in microchannels. *Phys. Rev. Lett.* **97,** 1–4 (2006).

10 Byun, D., Kim, J., Ko, H. S. & Park, H. C. Direct measurement of slip flows in superhydrophobic microchannels with transverse grooves. *Phys. Fluids* **20,** 113601 (2008).

[11] Choi, C. & Kim, C. Large slip of aqueous liquid flow over a nanoengineered superhydrophobic surface. *Phys. Rev. Lett.* **96,** 66001 (2006).

[12] Lauga, E. & Stone, H. A. Effective slip in pressure-driven Stokes flow. *J. Fluid Mech.* **489,** 55–77 (2003).

[13] Lee, C., Choi, C. H. & Kim, C. J. Structured surfaces for a giant liquid slip. *Phys. Rev. Lett.* **101,** 1–4 (2008).

[14] Park, H., Sun, G. & Kim, C. Superhydrophobic turbulent drag reduction as a function of surface grating parameters. *J. Fluid Mech.* **747,** 722–734 (2014).

[15] Daniello, R. J., Waterhouse, N. E. & Rothstein, J. P. Drag reduction in turbulent flows over superhydrophobic surfaces. *Phys. Fluids* **21,** 085103 (2009).

[16] Woolford, B., Maynes, D. & Webb, B. W. Liquid flow through microchannels with grooved walls under wetting and superhydrophobic conditions. *Microfluid. Nanofluidics* **7,** 121–135 (2009).

[17] Jung, Y. C. & Bhushan, B. Biomimetic structures for fluid drag reduction in laminar and turbulent flows. *J. Phys. Condens. Matter* **22,** 35104 (2010).

[18] Min, T. & Kim, J. Effects of hydrophobic surface on skin-friction drag. *Phys. Fluids* **16,** L55 (2004).

[19] Martell, M. B., Rothstein, J. P. & Perot, J. B. An analysis of superhydrophobic turbulent drag reduction mechanisms using direct numerical simulation. *Phys. Fluids* **22,** 065102 (2010).

[20] Jelly, T. O., Jung, S. Y. & Zaki, T. a. Turbulence and skin friction modification in channel flow with streamwise-aligned superhydrophobic surface texture. *Phys. Fluids* **26,** 095102 (2014).

[21] Woolford, B., Prince, J., Maynes, D. & Webb, B. W. Particle image velocimetry characterization of turbulent channel flow with rib patterned superhydrophobic walls. *Phys. Fluids* **21,** 085106 (2009).

[22] Verho, T., Bower, C., Andrew, P., Franssila, S., Ikkala, O. & Ras, R. H. Mechanically durable superhydrophobic surfaces. *Adv. Mater.* **23,** 673–8 (2011).

[23] Brinker, C. J., Branson, E., Kissel, D. J., Cook, A., Singh, S. Superhydrophobic coating. *USPatent*, US7485343 B1 (2008).

[24] Zhao, J., Du, X. & Shi, X. Experimental research on friction-reduction with super-hydrophobic surfaces. *J. Mar. Sci. Appl.* **6,** 58–61 (2007).

[25] Peguero, C. & Breuer, K. On Drag Reduction in Turbulent Channel Flow over Superhydrophobic Surfaces. *Adv. Turbul. XII* **132,** 233–236 (2009).

[26] Aljallis, E., Sarshar, M. A., Datla, R., Sikka, V., Jones, A. & Choi, C. Experimental study of skin friction drag reduction on superhydrophobic flat plates in high Reynolds number boundary layer flow. *Phys. Fluids* **25,** 025103 (2013).

[27] Gad-el-Hak, M. Comment on 'Experimental study of skin friction drag reduction on superhydrophobic flat plates in high Reynolds number boundary layer flow' [Phys. Fluids 25, 025103 (2013)]. *Phys. Fluids* **25,** 079101 (2013).

[28] Bidkar, R., Leblanc, L., Kulkarni, A. J., Bahadur, V., Ceccio, S. L. & Perlin, M. Skin-friction drag reduction in the turbulent regime using random-textured hydrophobic surfaces. *Phys. Fluids* **26,** 085108 (2014).

[29] Tian, H., Zhang, J., Wang, E., Yao, Z. & Jiang, N. Experimental investigation on drag reduction in turbulent boundary layer over superhydrophobic surface by TRPIV. *Theor. Appl. Mech. Lett.* **5,** 45–49 (2015).

[30] Srinivasan, S., Kleingartner, J. a, Gilbert, J. B., Cohen, R. E., Milne, A. J. B. & Mckinley, G. H. Sustainable Drag Reduction in Turbulent Taylor-Couette Flows by Depositing Sprayable Superhydrophobic Surfaces. *Phys. Rev. Lett.* **014501,** 1–5 (2015).

[31] Tian, H., Zhang, J., Jiang, N. & Yao, Z. Effect of hierarchical structured superhydrophobic surfaces on coherent structures in turbulent channel flow. *Exp. Therm. Fluid Sci.* **69,** 27–37 (2015).

[32] Zhang, J., Tian, H., Yao, Z., Hao, P. & Jiang, N. Mechanisms of drag reduction of superhydrophobic surfaces in a turbulent boundary layer flow. *Exp. Fluids* **56,** 179 (2015).

[33] Haibao, H., Peng, D., Feng, Z., Dong, S. & Yang, W. Effect of hydrophobicity on turbulent boundary layer under water. *Exp. Therm. Fluid Sci.* **60,** 148–156 (2015).

[34] Moaven, K., Rad, M. & Taeibi-Rahni, M. Experimental investigation of viscous drag reduction of superhydrophobic nano-coating in laminar and turbulent flows. *Exp. Therm. Fluid Sci.* **51,** 239–243 (2013).

[35] Farshad, F. F. & Pesacreta, T. C. Coated pipe interior surface roughness as measured by three scanning probe instruments. *Anti-Corrosion Methods Mater.* **50,** 6–16 (2003).

[36] Brennan, J. C., Fairhurst, D. J., Morris, R. H., McHale, G. & Newton, M. I. Investigation of the drag reducing effect of hydrophobized sand on cylinders. *J. Phys. D. Appl. Phys.* **47,** 205302 (2014).

[37] Brennan, J. C., Geraldi, N. R., Morris, R. H., Fairhurst, D. J., McHale, G. & Newton, M. I. Flexible conformable hydrophobized surfaces for turbulent flow drag reduction. *Sci. Rep.* **5,** 10267 (2015).

[38] Meinhart, C. D., Wereley, S. T. & Santiago, J. G. A PIV Algorithm for Estimating Time-Averaged Velocity Fields. *J. Fluids Eng.* **122,** 285 (2000).

[39] Kähler, C. J., Scharnowski, S. & Cierpka, C. On the uncertainty of digital PIV and PTV near walls. *Exp. Fluids* **52,** 1641–1656 (2012).

[40] Westerweel, J. & Scarano, F. Universal outlier detection for PIV data. *Exp. Fluids* **39,** 1096–1100 (2005).

[41] Stanislas, M., Perret, L. & Foucaut, J.-M. Vortical structures in the turbulent boundary layer: a possible route to a universal representation. *J. Fluid Mech.* **602,** 327–382 (2008).

[42] Saikrishnan, N., Marusic, I. & Longmire, E. K. Assessment of dual plane PIV measurements in wall turbulence using DNS data. *Exp. Fluids* **41,** 265–278 (2006).

[43] Martell, M. B., Perot, J. B. & Rothstein, J. P. Direct numerical simulations of turbulent flows over superhydrophobic surfaces. *J. Fluid Mech.* **620,** 31 (2009).

[44] Ou, J. & Rothstein, J. P. Direct velocity measurements of the flow past drag-reducing ultrahydrophobic surfaces. *Phys. Fluids* **17,** 0–10 (2005).

[45] Moser, R. D., Kim, J. & Mansour, N. N. Direct numerical simulation of turbulent channel flow up to Re 590 ⁄. *Phys. Fluids* **11,** 943–945 (1999).

[46] Schultz, M. P. & Flack, K. a. The rough-wall turbulent boundary layer from the hydraulically smooth to the fully rough regime. *J. Fluid Mech.* **580,** 381 (2007).

[47] Ghaemi, S. & Scarano, F. Counter-hairpin vortices in the turbulent wake of a sharp trailing edge. *J. Fluid Mech.* **689,** 317–356 (2011).

[48] Kim, J., Moin, P. & Moser, R. Turbulence statistics in fully developed channel flow at low Reynolds number. *J. Fluid Mech.* **177,** 133–166 (1987).

[49] Andreopoulos, J. & Bradshaw, P. Measurements of turbulence structure in the boundary layer on a rough surface. *Boundary-Layer Meteorol.* **20,** 201–213 (1981).

[50] White, C. M., Somandepalli, V. S. R. & Mungal, M. G. The turbulence structure of drag-reduced boundary layer flow. *Exp. Fluids* **36,** 62–69 (2004).

[51] Smith, C. R., Metzler, S. P. Characterization of low-speed streaks in the near-wall region of a turbulent boundary layer. *J. Fluid Mech.* **129,** 27–54 (1983).

[52] Kim, J. Physics and control of wall turbulence for drag reduction. *Philos. Trans. A. Math. Phys. Eng. Sci.* **369,** 1396–1411 (2011).

[53] Hunt, J.C.R., Wray, A.A., Moin, P. Eddies, Streams, and Convergence Zones in Turbulent Flows. *Res. Rep. CTR-S88, Cent. Turbul.* 193–208 (1988).

[54] Sheng, J., Malkiel, E. & Katz, J. Buffer layer structures associated with extreme wall stress events in a smooth wall turbulent boundary layer. *J. Fluid Mech.* **633,** 17–60 (2009).

[55] Maynes, D., Jeffs, K., Woolford, B. & Webb, B. W. Laminar flow in a microchannel with hydrophobic surface patterned microribs oriented parallel to the flow direction. *Phys. Fluids* **19,** 93603 (2007).